A new diagnostic of air-sea interaction reveals ocean control of turbulent heat flux in the South Asian Summer Monsoon

Alex Kinsella[a] and Amala Mahadevan[a]

[a] *Department of Physical Oceanography, Woods Hole Oceanographic Institution*

This manuscript is a non-peer reviewed preprint submitted to EarthArXiv on April 2, 2026. It is currently under review at the Journal of Climate.

Corresponding author: Alex Kinsella, alex.kinsella@whoi.edu

ABSTRACT: Air-sea interaction plays a central role in the South Asian summer monsoon, with processes such as surface turbulent heat fluxes, upper ocean mechanical mixing, surface buoyancy forcing, and surface moisture fluxes providing bridges between the ocean and atmosphere. The air-sea heat flux responds to internal variability in the ocean and atmosphere, as well as feedbacks arising from their interaction. Depending on whether SST drives turbulent heat flux or vice-versa, one may diagnose the air-sea heat exchange as being in an ocean-controlled regime or an atmosphere-controlled regime. We develop a method to quantify the air-sea interaction regime at each location and yearday by analyzing lagged correlations between SST and turbulent heat flux records from satellite data or reanalysis. We apply this method to the northern Indian Ocean and find that the basin exhibits a coherent shift from atmosphere control to ocean control during the summer monsoon onset and a return to atmosphere control during the monsoon retreat. This finding emphasizes the importance of oceanic processes such as entrainment and advection in monsoon dynamics. The Arabian Sea exhibits a more pronounced shift between atmosphere and ocean control than the Bay of Bengal, suggesting the importance of upper-ocean stratification and mixing in determining the turbulent heat flux in response to the monsoon wind. We find good agreement between the regimes diagnosed from blended satellite products and reanalysis, showing robustness of the results across datasets. Our method may provide a useful diagnostic for verifying air-sea interaction within coupled models of the ocean and atmosphere.

1. Introduction

The onset of the South Asian summer monsoon, the defining phenomenon of the northern Indian Ocean basin, profoundly alters the flow and thermodynamic structure of the regional ocean and atmosphere (Gadgil 2003; Schott and McCreary Jr 2001). This shift adjusts the air-sea heat fluxes as well: as the Somali Jet and related monsoon winds energize over the basin, latent heat flux to the atmosphere sharply increases, while the thick clouds filling the region decrease downwelling shortwave radiation (Weller et al. 2016). Correctly modeling the physics of the monsoon onset and subsequent rainy season is critical to precipitation forecasts during the core agricultural growing season in central India and surrounding South Asian countries (Goswami et al. 2016).

While winds and rainfall define the monsoon, the ocean plays an important role in the coupled system, providing copious moisture, latent energy, and a spatial temperature contrast. All of these contributions to monsoon activity are mediated by the sea surface temperature (SST, with daily anomaly T_s) in the Northern Indian Ocean (Vecchi and Harrison 2002). The SST is controlled by a variety of processes, including turbulent (latent + sensible) and radiative (shortwave + longwave) surface heat fluxes, advection, upwelling, entrainment, and the mixed layer heat capacity (Shenoi et al. 2002). Within the surface heat fluxes, we focus in this work on the turbulent heat flux (THF, with daily anomaly Q_{turb}). This is the combined heat exchange accomplished by evaporation (latent heat flux) and conduction (sensible heat flux). A particularly important process in the northern Indian Ocean is upper ocean mixing, which combines the effects of wind forcing, buoyancy forcing, wave-driven mixing, turbulence, and entrainment at the base of the mixed layer. These processes are all active during the monsoon onset and differ between the Arabian Sea to the west and the Bay of Bengal to the east. The upper ocean in the Arabian Sea is weakly stratified and mixes easily from wind or surface cooling, while the Bay of Bengal is strongly stratified due to freshwater input by river runoff and rain, resisting mixing (Thakur et al. 2019). In both cases, upper ocean mixing (or lack thereof) is of first-order importance in determining the sea surface temperature in the region. Mesoscale and submesoscale eddies and frontal dynamics are additionally important to the air-sea interaction, particularly in the Bay of Bengal and western Arabian Sea (Goswami et al. 2016).

The THF is controlled by additional variables from both the ocean and atmosphere sides of the air-sea interface, such as sea state, surface currents, windspeed, temperature, and humidity. In different regions and seasons and at a particular lengthscale and timescale, the THF anomaly Q_{turb}

may be influenced primarily by oceanic variability, atmospheric variability, or a combination of the two. Additionally, both sides of the interface may provide feedbacks on Q_{turb}. Generally, when air-sea interaction is ocean controlled, variability in SST anomaly T_s is caused by internal ocean processes rather than atmospheric forcing, and variability in Q_{turb} is in turn driven by changes in T_s. These two conditions are not always met simultaneously, but it is found that they tend to occur together. Conversely, we consider the air-sea interaction to be in atmospheric control when variability in T_s is caused primarily by Q_{turb}, and variability in Q_{turb} is caused primarily by variability in surface air temperature and windstress.

In this work, we are motivated by two key questions about the control of THF in the northern Indian Ocean:

1. To what extent do oceanic processes control Q_{turb} in the northern Indian Ocean before, during, and after the summer monsoon season?

2. How do the Bay of Bengal and Arabian Sea differ in their ocean/atmosphere control of Q_{turb}?

The degree of ocean and atmosphere control of Q_{turb} is determined by variability on either side of the air-sea interface, which is difficult to measure with sufficient spatiotemporal resolution, particularly in the subsurface ocean. On the other hand, we have ready access to T_s and Q_{turb} from satellite data and blended reanalysis products. By studying the lagged relationships between T_s and Q_{turb} and comparing to a simple model with known underlying oceanic and atmospheric drivers, we deduce the ratio of atmosphere to ocean control of Q_{turb}, and thus the air-sea interaction regime (ASI regime). To accomplish this, we employ an analysis based on the T_s-Q_{turb} lagged cross correlation curves introduced by (Frankignoul and Hasselmann 1977) and used in many subsequent studies (Frankignoul 1985; Frankignoul and Kestenare 2002; von Storch 2000; Wu et al. 2006; Park et al. 2005; Bishop et al. 2017; Laurindo et al. 2022). These lagged correlations are used to quantify the strength of the Q_{turb} feedback to SST anomalies (Frankignoul et al. 1998; Frankignoul and Kestenare 2002; Frankignoul et al. 2004).

Given an SST anomaly time series $T_s(t)$ and THF anomaly time series $Q_{\text{turb}}(t)$, we form the lagged correlation at lag l as

$$C_{T_s,Q_{\text{turb}}}(l) = \frac{\operatorname{cov}(T_s(t), Q_{\text{turb}}(t+l))}{\sigma_{T_s}\sigma_{Q_{\text{turb}}}} \tag{1}$$

where σ denotes the standard deviation of a time series. We define positive lag $l > 0$ to correspond to T_s lagging Q_{turb}. In this work, we use daily time series, with t and l in days. This calculation gives us a series of correlation coefficients as a function of the lag at every location. We compare these correlation curves from observations to those obtained from a stochastic model, where underlying ocean/atmosphere variability is explicitly known, to extract the underlying forcing regimes.

Calculating lagged correlations of Q_{turb} with SST *tendency* anomaly ($\mathrm{d}T_s/\mathrm{d}t$) gives additional information about the ocean or atmosphere control of air-sea interaction (Bishop et al. 2017). The lagged correlation curves show coherent symmetry properties about zero lag that may be used to diagnose ASI regimes (Fig. 1). In an ocean-controlled regime, the daily T_s-Q_{turb} correlation curve (plotted as a function of lag) tends to be symmetric about zero lag, while the $\mathrm{d}T_s/\mathrm{d}t$-$Q_{\text{turb}}$ correlation tends to be antisymmetric about zero lag, as shown by (Bishop et al. 2017) on the monthly timescale. In an atmosphere-controlled regime, these symmetry properties are reversed. Given these defining symmetry properties of the two ASI regimes, we can compute the relative proportions of ocean and atmosphere control. Because we are interested in the evolution of the northern Indian Ocean heat fluxes over shorter timescales, particularly the weekly timescales of the monsoon onset, we compute the *daily* cross correlation. We introduce a novel algorithmic computation of an air-sea interaction regime diagnostic parameter P_o on a daily basis, including statistical testing of the correlations.

Our ability to make conclusions about the underlying variability driving air-sea interaction from lagged correlations comes from studying the resulting curves in the case of simple models of air-sea interaction. There are two stochastic models often used for this purpose: the single upper ocean temperature ODE of Frankignoul et al. (1998) (hereafter FCL98), employed, for example, by Laurindo et al. (2022), and the coupled ocean and atmosphere ODE system of Barsugli and Battisti (1998), implemented by Wu et al. (2006), Bishop et al. (2017), and others. In our case, lagged correlation curves from FCL98 better fit the observations, so we use this model to provide interpretation for our results.

The rest of this paper is structured as follows. Section 2 describes our methods, including the stochastic model and its use to interpret air-sea interaction regimes. We then describe the processing and regression used to diagnose ASI regimes from observational datasets and reanalysis. We describe our results in Section 3, where we investigate the annual cycle of ASI regimes in the northern Indian Ocean and look at the effects of surface wind stress and stratification. We discuss our results in Section 4, with consideration of oceanic and radiative processes as well as applications to models before concluding in Section 5.

2. Methods

In this section, we first explain the FCL98 model used to interpret our results and then discuss our ASI regimes algorithm in the context of observational datasets and model output.

a. Stochastic Model

To interpret correlations between T_s and Q_{turb} time series, we employ a stochastic air-sea interaction model (Frankignoul et al. 1998):

$$\frac{\mathrm{d}T_s}{\mathrm{d}t} = -\lambda_s(T_s - T_a) - \lambda_r T_s + Q_o \ , \tag{2}$$

where T_s is upper ocean temperature anomaly, λ_s is the turbulent heat flux feedback parameter, T_a is the surface air temperature anomaly, λ_r is the longwave radiative feedback parameter, and Q_o is intrinsic oceanic forcing. Anomalies are typically taken with respect to monthly climatology, but for our application we use a daily climatology.

The atmospheric noise term $T_a = \omega_a r_a$ is a daily Gaussian white noise variable with strength ω_a in K and Gaussian white noise process r_a with mean 0 and standard deviation 1. The ocean forcing $Q_o(t)$ is an AR(1) red-noise process defined by:

$$Q_o(t) = \phi Q_o(t-1) + \sqrt{1-\phi^2}\,\omega_o r_o \, , \tag{3}$$

where ω_o is the strength of the forcing in W m^{-2}, r_o is a Gaussian white noise process with mean 0 and standard deviation 1, and $\phi = e^{-1/\tau}$, where τ is the memory timescale. See Table 1 for the parameters used in this work. We perform a series of model runs, holding the ocean forcing magnitude ω_o constant and using 60 evenly-spaced atmospheric noise strengths ω_a between 0 and 10 K to represent a range of ASI regimes.

Q_{turb} is calculated from the resulting time series as $Q_{\text{turb}} = \lambda_s(T_s - T_a)$, using a positive-upward sign convention. The feedback parameters are chosen as $\lambda_s = 30$ W m^{-2} K^{-1} and $\lambda_r = 5$ W m^{-2} K^{-1}, modifying the parameters used by Frankignoul et al. (1998) for our tropical conditions. Because our method relies only on the symmetry properties of the correlation curves, it is not sensitive to this parameter choice.

Density ρ_0 (Kg m^{-3})	Heat Capacity c_p (J Kg^{-1} K^{-1})	Mixed layer depth H (m)	Turbulent feedback λ_s (W m^{-2} K^{-1})	Radiative feedback λ_r (W m^{-2} K^{-1})	Stochastic timescale τ (days)	Oceanic forcing ω_o (W m $^{-2}$)	Atmospheric forcing ω_a (K)
1025	3900	20	30	5	0.1	100	0–10

TABLE 1. Parameters used across model runs.

This model gives rise to lagged T_s-Q_{turb} correlation curves shown in Fig. 1, with ocean control exhibiting T_s-Q_{turb} correlations symmetric about zero lag and $\frac{\mathrm{d}T_s}{\mathrm{d}t}$-$Q_{\text{turb}}$ correlations antisymmetric about zero lag, and the atmosphere control case with the opposite symmetry properties. This connection between the lagged symmetry properties and the underlying variability in the model is the basis for inferring ASI regimes from observational data, where the correlation symmetry properties may be readily measured.

b. ASI Regime Calculation

We compute observational T_s-Q_{turb} correlations based on the OAFlux 1-degree product (Yu and Weller 2007), which blends satellite measurements and reanalysis to estimate 10-meter windspeeds and Q_{turb} using the COARE algorithm (Edson et al. 2013). Because OAFlux is optimized for use with the NOAA OISSTv1 SST product (Reynolds et al. 2007), we use this product for the lagged correlation calculations. Our analysis period is 1985-2020. To test the robustness of the results, we perform the same analysis with ERA5 reanalysis (Hersbach et al. 2020) over the same timeframe.

Computing the ASI regimes is done by the following three steps:

1. Dataset Processing First, we obtain the three variables of interest: T_s, $\frac{\mathrm{d}T_s}{\mathrm{d}t}$, and Q_{turb}, with daily $\mathrm{d}T_s/\mathrm{d}t$ calculated as a second-order central difference of the daily T_s record. We calculate a daily climatology for each based on the available record using the method of Hobday et al. (2016), which was developed for studying marine heat waves. For a given day of the year, across all years in the time series, values are averaged in an 11-day rectangular window (5 days on either side of the day of interest). After computing the windowed average for each day, a 30-day moving mean

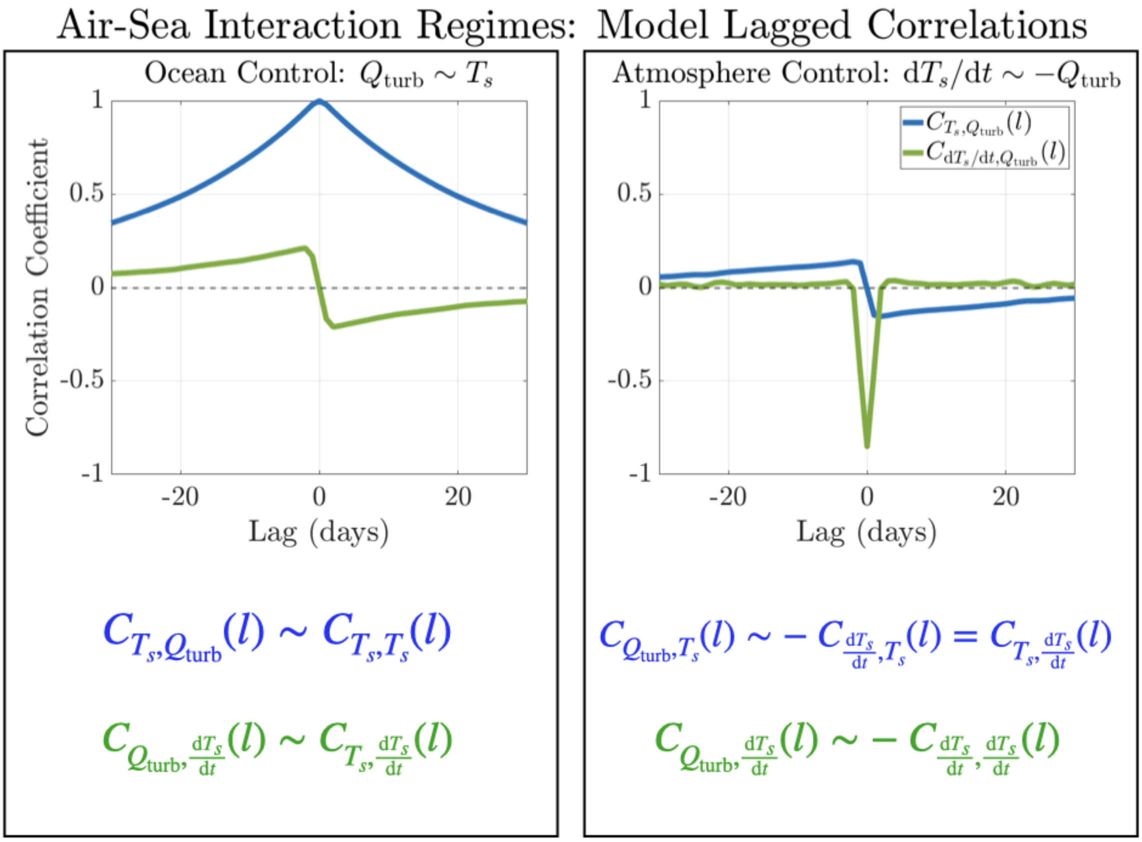

FIG. 1. Characteristic lagged correlation curves between turbulent heat flux anomaly Q_{turb} and SST anomaly T_s (blue) and its tendency $\mathrm{d}T_s/\mathrm{d}t$ (green) computed from the simple stochastic model of FCL98. In the ocean control case (left), the T_s-Q_{turb} curve is symmetric about zero lag, while the $\mathrm{d}T_s/\mathrm{d}t$-$Q_{\mathrm{turb}}$ curve is antisymmetric about zero lag. These symmetry properties arise from the linearized relationship $Q_{\mathrm{turb}} \sim T_s$ that defines ocean control, substituted in the lagged correlation calculations (bottom left); the lagged correlation of a variable with itself is symmetric about zero lag, while a lagged correlation of a variable with its own tendency is antisymmetric about zero lag. Similar reasoning applies to the atmosphere control side (right), defined by the relation $\mathrm{d}T_s/\mathrm{d}t \sim -Q_{\mathrm{turb}}$.

filter is applied to the result to reduce high-frequency noise. This procedure results in a daily climatology of the variable of interest indexed by spatial location and calendar day. We subtract the daily climatology from the time series to obtain daily anomalies of each variable. Computing the air-sea interaction regime parameter with the full time series, rather than the anomalies, makes

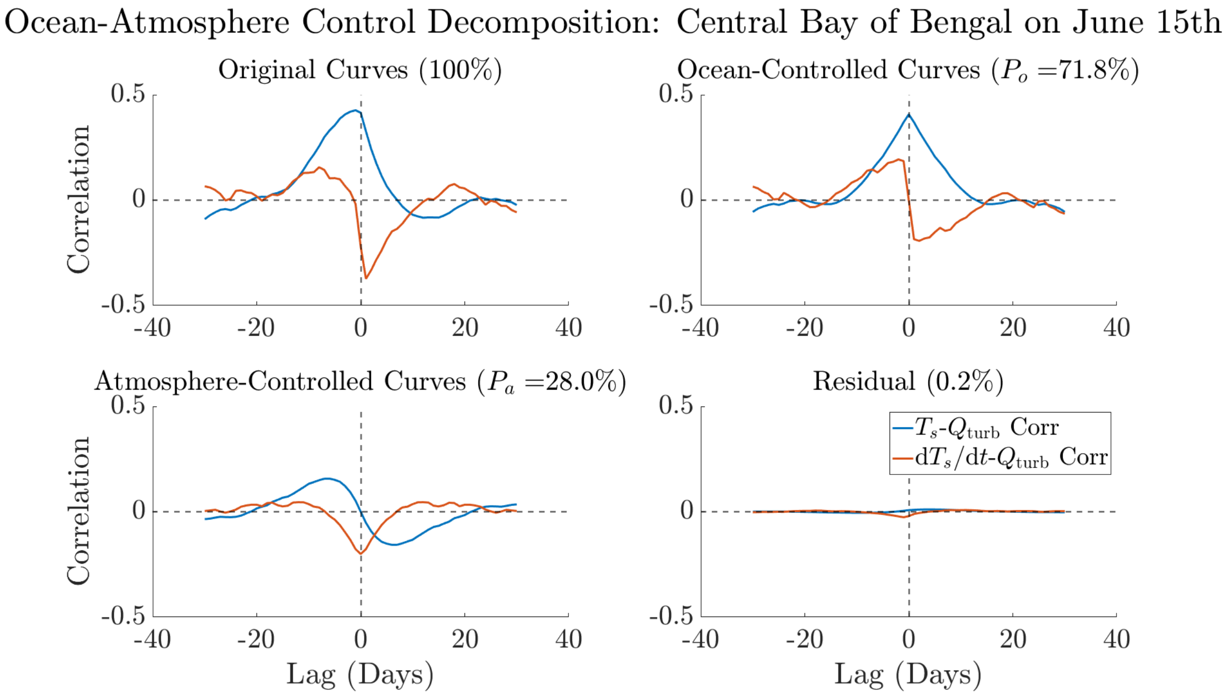

FIG. 2. Decomposition of lagged correlation curves into an atmosphere-controlled part, an ocean-controlled part, and a residual. This example uses the daily lagged correlations for a point in the central BoB (16.5N,89.5E) centered on June 15th over 35 years (1985-2020). The decomposition reveals that the regime is primarily ocean-controlled (P_o = 73.8%) with a contribution from the atmosphere (26.0%). The small residual (0.2%) indicates a good fit.

only a small difference in our results, with no qualitative change in our interpretation. We use the anomaly time series to remain consistent with previous calculations of air-sea interaction regimes.

For each grid point and each day of the calendar year, we calculate two lagged correlation series: 1) T_s with Q_{turb} and 2) $\frac{\mathrm{d}T_s}{\mathrm{d}t}$ with Q_{turb}. This is done using Equation 1 with a sliding 30-day rectangular window and lags from -30 to 30 days. The window for Q_{turb} is fixed around the calendar day of interest, while the window for T_s is slid up to 30 days leading or lagging the window for Q_{turb}. Windowed time series for all years are concatenated and the cross correlation is calculated. The result of this procedure is a collection of correlation coefficients and p-values indexed by longitude, latitude, lag, and yearday.

2. Statistical Testing The lagged correlation curves from which our ASI regime parameter is constructed are an inherently statistical test, with not all correlations statistically significant. We use a bootstrapping method to determine that very few of our daily lagged correlation curves are the result of noise. In our parameter calculation, we de-emphasize less significant results using p-values that are corrected for autocorrelation and multiple testing. For more details, see the Appendix. To our knowledge, this is the first time that such statistical tests have been applied to ASI regime analyses.

3. Regime Parameter Calculation To identify the ASI regime at a grid point as being atmosphere- or ocean-controlled on a given day of the year, we use the symmetry properties of the lagged correlation curves (Fig. 1). For a fixed location and yearday, we construct correlation curves $C_{T_s,Q_{\mathrm{turb}}}(l)$ and $C_{\frac{\mathrm{d}T_s}{\mathrm{d}t},Q_{\mathrm{turb}}}(l)$, where l is the lag in days (Equation 1) and decompose these into their symmetric and antisymmetric parts as:

$$C_{T_s,Q_{\mathrm{turb}},\mathrm{sym}}(l) = \frac{1}{2}(C_{T_s,Q_{\mathrm{turb}}}(l) + C_{T_s,Q_{\mathrm{turb}}}(-l)) \tag{4}$$

$$C_{T_s,Q_{\mathrm{turb}},\mathrm{asym}}(l) = \frac{1}{2}(C_{T_s,Q_{\mathrm{turb}}}(l) - C_{T_s,Q_{\mathrm{turb}}}(-l)) \tag{5}$$

$$C_{\mathrm{d}T_s/\mathrm{d}t,Q_{\mathrm{turb}},\mathrm{sym}}(l) = \frac{||C_{\mathrm{d}T_s/\mathrm{d}t,Q_{\mathrm{turb}}}||}{2||C_{T_s,Q_{\mathrm{turb}}}||}(C_{\mathrm{d}T_s/\mathrm{d}t,Q_{\mathrm{turb}}}(l) + C_{\mathrm{d}T_s/\mathrm{d}t,Q_{\mathrm{turb}}}(-l)) \tag{6}$$

$$C_{\mathrm{d}T_s/\mathrm{d}t,Q_{\mathrm{turb}},\mathrm{asym}}(l) = \frac{||C_{\mathrm{d}T_s/\mathrm{d}t,Q_{\mathrm{turb}}}||}{2||C_{T_s,Q_{\mathrm{turb}}}||}(C_{\mathrm{d}T_s/\mathrm{d}t,Q_{\mathrm{turb}}}(l) - C_{\mathrm{d}T_s/\mathrm{d}t,Q_{\mathrm{turb}}}(-l)) \tag{7}$$

The normalization factor in front of the SST tendency terms is required so that the SST and tendency correlations are weighted equally in the computation to follow. The norms indicate L^2 norms of the correlation lag series regarded as a vector. Each of these component correlations is then L^2-normalized (denoted below by a caret) and set up as a matrix equation:

$$\begin{cases} C_{T_s,Q_{\mathrm{turb}}} = b_o\hat{C}_{T_s,Q_{\mathrm{turb}},\mathrm{sym}} + b_a\hat{C}_{T_s,Q_{\mathrm{turb}},\mathrm{asym}} + r_{T_s} \\ C_{\mathrm{d}T_s/\mathrm{d}t,Q_{\mathrm{turb}}} = b_a\hat{C}_{\mathrm{d}T_s/\mathrm{d}t,Q_{\mathrm{turb}},\mathrm{sym}} + b_o\hat{C}_{\mathrm{d}T_s/\mathrm{d}t,Q_{\mathrm{turb}},\mathrm{asym}} + r_{\mathrm{d}T_s/\mathrm{d}t} \end{cases} \tag{8}$$

where we have now suppressed the lag arguments and introduced coefficients b_o and b_a and residuals r_{T_s} and $r_{\mathrm{d}T_s/\mathrm{d}t}$, with coefficients satisfying $b_o + b_a = 1$. Equations 8 are solved by least squares with the constraint that the coefficients b_o and b_a are positive. We additionally introduce a statistical weighting matrix in our fit to de-emphasize low-confidence correlations (see the Appendix for details).

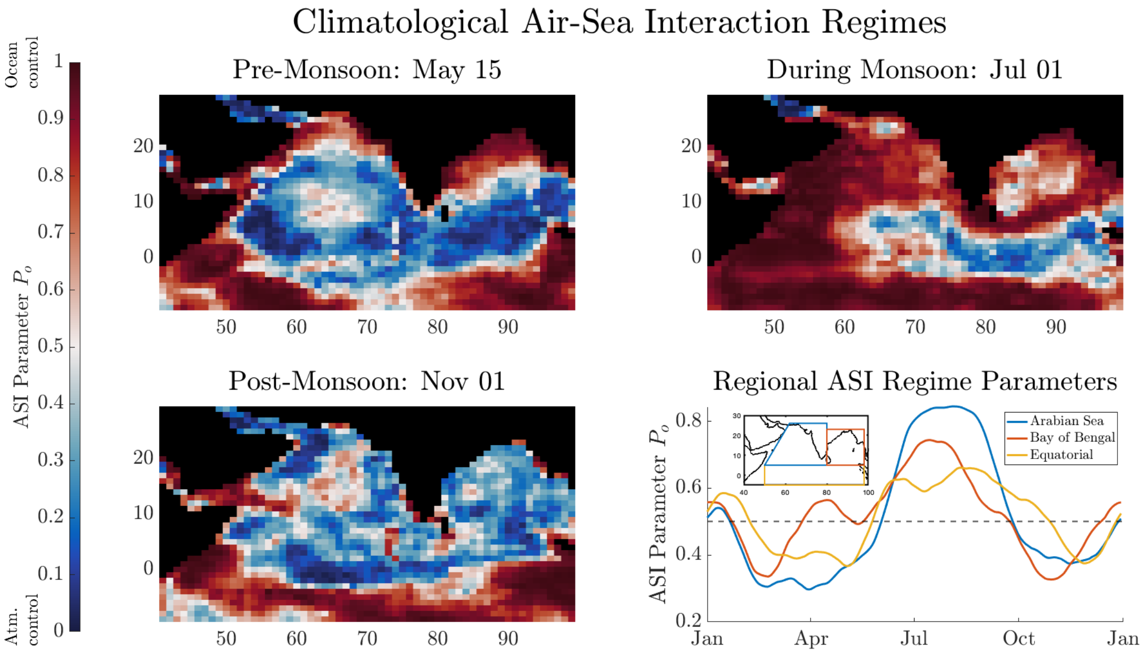

FIG. 3. A comparison of the pre-monsoon, monsoon, and post-monsoon ASI regimes from OAFlux data. In the pre-monsoon season, the majority of the interior basin is atmosphere controlled, with the exception of the ocean margins, particularly in the northern BoB. During the monsoon, the region becomes primarily ocean-controlled with the exception of a tongue in the equatorial region. In the post-monsoon season, the northern Indian Ocean returns to primarily atmosphere control, with ocean control persisting only in the southern tropical Indian Ocean. The bottom right panel shows the regional average of the ASI parameter over the course of the year, highlighting the more dramatic seasonal swing in the Arabian Sea than in the Bay of Bengal.

The degree of ocean and atmosphere control is then determined by $P_o = b_o^2/(b_o^2 + b_a^2)$ and $P_a = b_a^2/(b_o^2 + b_a^2)$, where $P_o + P_a = 1$. We use P_o as our ASI regime parameter: the regime is fully ocean-controlled when $P_o = 1$ and it is fully atmosphere-controlled when $P_o = 0$. See Fig. 2 for an example of the algorithm applied to the central Bay of Bengal in June.

3. Results

a. Seasonal Variability of ASI Regimes

Using the algorithm described in Section 2, we compute daily ASI regimes over the northern Indian Ocean from the OAFlux blended satellite product. The resulting ASI regimes exhibit

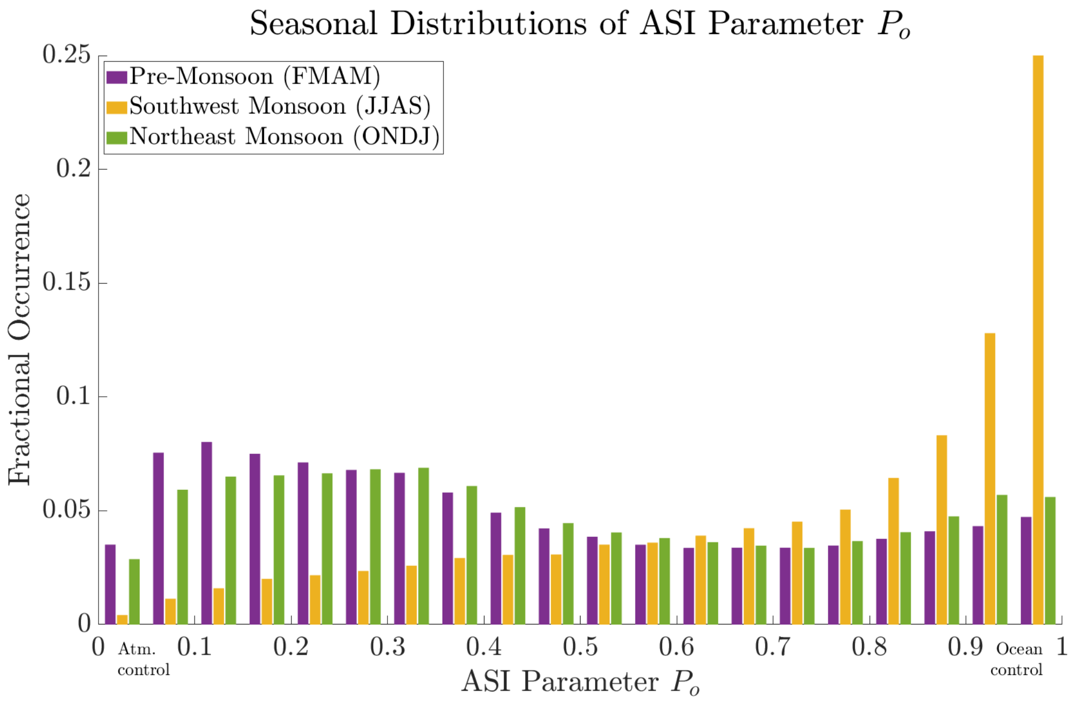

FIG. 4. Histograms showing the seasonal distribution of ASI regime parameters during the pre-monsoon season (FMAM), the southwest monsoon season (JJAS), and the northeast monsoon season (ONDJ). The parameters are those in the combined Arabian Sea and Bay of Bengal regions, as shown by the dashed polygons in Fig. 5b.

strong seasonal and subseasonal variability during monsoon onset, peak, and retreat (Fig. 3). See Supplemental Video V1 for an animation of the daily ASI regimes.

In the April-May pre-monsoon season, THF over the interior of the northern Indian Ocean basin is largely controlled by the atmosphere, while ocean control is limited to the margins and the tropical south Indian Ocean. During the monsoon onset, there THF transitions rapidly from an atmosphere-controlled regime to an ocean-controlled regime over the entire basin with a timescale of approximately 14 days. Because this is a climatological calculation, the transition is averaged across seasons such that it is smoothed in space and time; in a given year, the regime transition is faster in time and patchier in space than the climatology. With the monsoon onset, ocean control extends into the interior of the basin, covering the entire area except for a tongue in the eastern and central equatorial region (Fig. 3b). Ocean control is sustained throughout the summer season until the retreat of the monsoon, when the region returns to being predominantly atmosphere controlled on a similar timescale of approximately 14 days.

During the late northeast monsoon season (December and January), the THF transitions again to ocean control over much of the region, although the magnitude of the change is weaker than the summer monsoon, with the area-averaged regime parameters showing split ocean-atmosphere control rather than the strong ocean control exhibited during the summer season (Fig. 3d). The northeast monsoon ocean control of THF is strongest in the western equatorial region and extends in a band northeastward to the Bay of Bengal. This ocean controlled patch shrinks during the pre-summer monsoon season, beginning in February, as the region returns to almost entire atmosphere control of THF.

The pre-monsoon spatial map in Fig. 3a shows an increased ocean control around the basin margins compared to the interior. Near-shore pixels (those within two 1°×1° grid boxes, or approximately 200km of the coast) have average ocean control $P_o = 0.59$ during MAM, while those in the interior have average $P_o = 0.44$ during this season. We expect coastal processes such as upwelling and Kelvin waves to become important at the coast, particularly in the pre-monsoon season, increasing the ocean control of THF along the margins (Rao et al. 2010; Abbott and Mahadevan 2024). This effect is particularly strong in the Bay of Bengal (Fig. 3d), where the transition to ocean control begins around the margins in April and spreads to the interior with the onset of the monsoon.

The drastic difference between the southwest monsoon season (JJAS) and the other seasons is apparent in the seasonal histograms of ASI regime parameters (Figure 4) calculated for the combined Arabian Sea and Bay of Bengal.

b. Spatial Variability and Windstress Correlation

The timescale of monsoon regime transition varies spatially, being as fast as 14 days in the Arabian Sea. The Bay of Bengal and equatorial region undergo a slower transition, with ocean control of their area-averaged regimes ramping up and down on a seasonal timescale (Fig. 3d). The Bay of Bengal ASI regime parameter has a smaller variation throughout the year than that of the Arabian Sea, becoming less atmosphere-controlled during the inter-monsoon seasons and less ocean-controlled during the summer monsoon. The Bay of Bengal also begins to return to atmosphere control earlier than the Arabian Sea, with its ocean control peaking near the beginning of July and steadily decreasing thereafter. This is in part due to the differing temperature-salinity

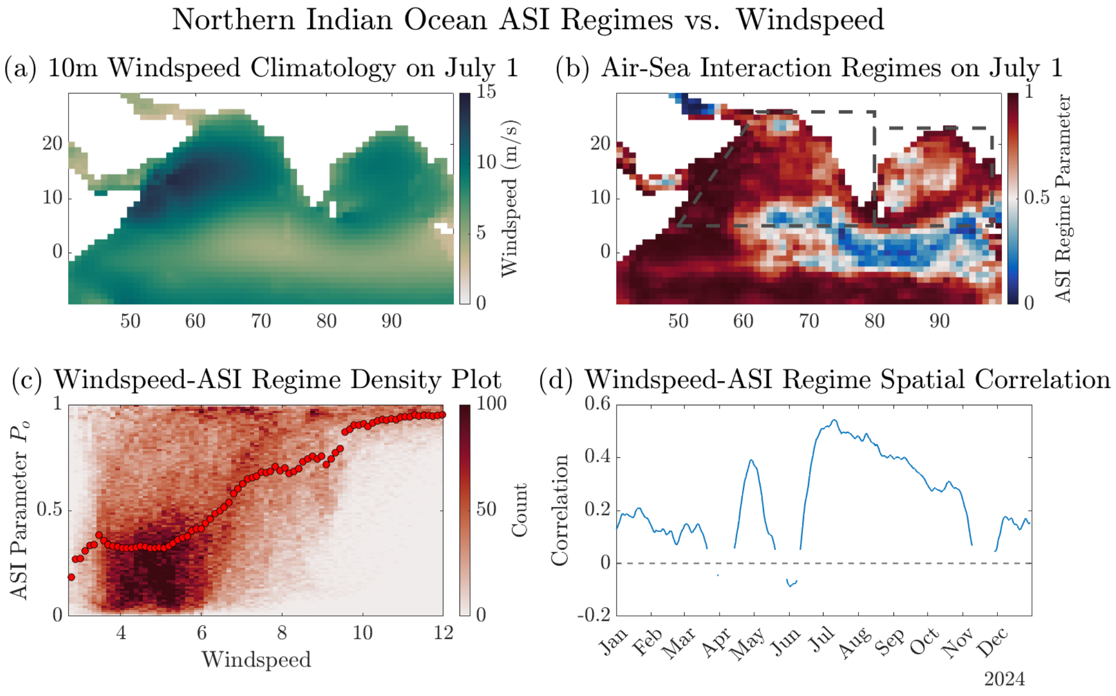

Fig. 5. (a) Climatology of 10m windspeed on July 1 over the Northern Indian Ocean. (b) ASI regimes over the NIO for the same date. Gray dashed polygons show the regions used for the Arabian Sea and Bay of Bengal in the following panel. (c) 2D histogram of ASI regime vs. windspeed for the Arabian Sea and Bay of Bengal combined. Shading denotes counts of occurrence within a bin and red dotted line shows the median regime parameter at each windspeed. (d) Pearson correlation coefficient between 10m wind speed and ASI regimes at the daily, 1-degree scale. Gaps in the time series denote days when the correlation is not statistically significant according to a Benjamini-Hochberg test with false discovery rate of 0.1

.

structures of the upper ocean in these two seas; the strong salinity-controlled stratification and frequent temperature inversions in the Bay of Bengal decrease the effectiveness of surface wind stress at controlling sea surface temperature through mixing and mixed layer entrainment (Shenoi et al. 2002). The mixed layer depth is often defined by salinity and overlies a barrier layer which is as warm as the mixed layer. Additionally, the persistence of the winds differs between the two sub-basins: the Arabian Sea experiences long spells of constant, moderate-to-strong winds, while the Bay of Bengal exhibits more episodic wind bursts (Abbott and Mahadevan 2024).

A feature of the ASI regimes is that strong wind stress, while originating in the atmosphere, is often correlated with an ocean-controlled ASI regime (Fig. 5ab). Figure 5c shows a 2D histogram of the ASI regime parameter and 10m windspeed over the Arabian Sea and Bay of Bengal, with the median in each windspeed bin (red dots) increasing with increasing windspeeds. The windspeed climatology and ASI regimes are found to be significantly spatially correlated at the daily, 1°×1° scale, up to a maximum correlation coefficient of $R = 0.55$ during the summer monsoon season (Fig. 5d). Causative links include, for example, wind-driven entrainment and mixing de-emphasizing the role of surface heat fluxes on the SST tendency and increasing ocean control of the turbulent heat fluxes. On the other hand, increased windstress strengthens turbulent heat fluxes so that they become more important in the SST budget, increasing atmosphere control. Increasing wind stress induces the following competing effects on the regime:

1. Mechanical mixing and surface heat loss both lead to ocean mixing, increasing ocean control
2. Positive windstress curl generates upwelling, increasing ocean control
3. Wind-induced currents advect ocean heat, increasing ocean control
4. Increased turbulent heat flux enhances atmosphere control

The balance between these effects is expected to be controlled in part by upper-ocean stratification. A strongly stratified ocean will have suppressed mixing, reducing the role of oceanic processes in controlling the SST. A weakly stratified ocean will respond with vigorous mixing to the same forcing.

The spatial correlation between windspeed and the ASI regime parameter is statistically significant over much of the year, but the correlation is largest during the summer monsoon season (Fig. 5d), suggesting that wind plays a smaller role in setting the regimes during other seasons. This is reflected by the larger spread about the median at low windspeeds in Fig. 5c, representing more heterogeneity in the ASI regime and a substantially smaller effect of the wind.

c. Consistency Across Datasets

To test the robustness of our results, we compare the OAFlux-derived ASI regimes to those computed from ERA5 0.25-degree reanalysis for the same time period, 1985-2020 (Hersbach et al. 2020). The results qualitatively agree, with a transition from atmosphere to ocean control during the monsoon onset over the non-equatorial portion of the basin (Fig. 6). A correlation between OAFlux- and ERA5-based ASI regime parameters at the daily, 1°×1° scale across all grid points

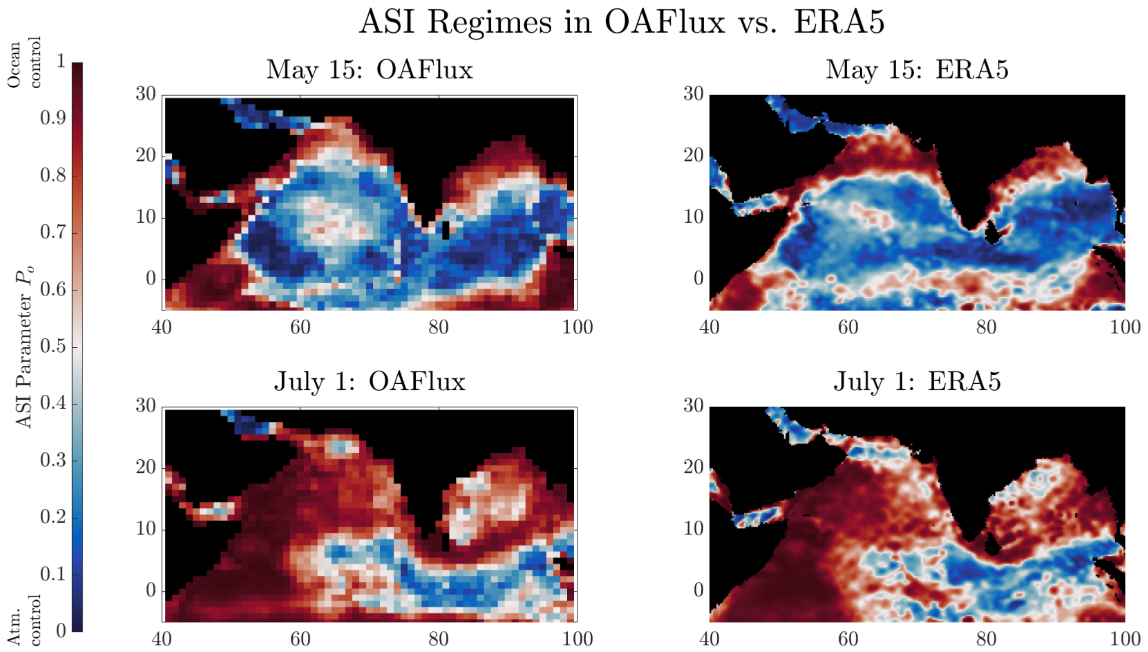

FIG. 6. ASI regime parameter values on May 15 and July 1 derived from OAFlux (1°×1°) and ERA5 (0.25°×0.25°) datasets from 1985-2020.

and yeardays gives $R^2 = 0.63$, confirming a broad-scale agreement, while spatial and temporal details in ASI regimes differ between the two products. For example, the ERA5-based regimes transition from ocean to atmosphere control in the late winter, earlier than in the OAFlux-based regimes (Supplemental Video V1). The OAFlux regimes also show weaker ocean control in the Bay of Bengal during the summer monsoon season, particularly during August, and the Bay begins to transition to atmosphere control earlier than in the ERA5 regimes.

The consistent spatial and seasonal patterns of ASI regimes derived from both OAFlux and ERA5 suggest that the core results are robust, despite known biases in each dataset. OAFlux is subject to uncertainties in regions of weak winds, heavy rainfall, and near coastlines (Yu and Weller 2007; Bentamy et al. 2017), while ERA5 fluxes reflect biases in model physics and data assimilation (Hersbach et al. 2020). However, our methodology emphasizes the symmetry of lagged correlations, which depends more on interaction structure than on flux magnitude, reducing sensitivity to absolute biases.

4. Discussion

Applying our methodology to the northern Indian Ocean has shown that the THF over the basin becomes strongly ocean-controlled during the summer monsoon season and that there is high spatial correlation between climatological windspeed and the ASI regime during the summer monsoon. Ocean control corresponds to a state where the anomalous mixed layer heat budget is primarily controlled by terms other than the turbulent heat flux. To determine the origin of our results, we explore the influence of ocean processes and atmospheric radiation in the heat budget.

a. Influence of Ocean Processes

Ocean processes contributing to the mixed layer heat budget primarily include ocean advection, where water is transported through temperature gradients, and mixing, where water parcels of differing temperatures are combined, especially at the base of the mixed layer. The seasonal importance of oceanic processes in the mixed layer heat budget of the northern Indian Ocean is emphasized by previous analyses (Montégut et al. 2007; Rao and Sivakumar 2000; Prasad 2004; Jain et al. 2021). The comparative mixed layer heat budget analysis of Shenoi et al. (2002) found that oceanic processes are particularly important during the summer monsoon season, with their contribution exceeding that of surface fluxes in the Arabian Sea. In the Bay of Bengal, oceanic processes were found to be of similar magnitude to surface fluxes from June-January. More recent heat budget analyses have come to similar qualitative conclusions. For example, the mooring-based study of Thangaprakash et al. (2016) showed that upper ocean heat fluxes due to oceanic processes are comparable to surface heat fluxes in the Bay of Bengal, particularly in the northern bay (Thakur et al. 2019). The role of subsurface mixing in the Bay of Bengal was further emphasized by Warner et al. (2016), who found from direct measurements that ocean mixing dominates SST cooling during the summer monsoon, when surface heat fluxes alone would lead to warming. These findings are in line with our results that the air-sea interaction regime is ocean-controlled during the southwest monsoon season and atmosphere-controlled in the pre-monsoon and northeast monsoon seasons.

The lagged correlation curves between SST and surface fluxes are known to depend on scale (Small et al. 2008; Bishop et al. 2017; Laurindo et al. 2022). For instance, SST and windstress magnitude tend to be positively correlated on small scales ($< 2°\times2°$ spatial resolution), where high SST increases gustiness, while they are negative on large scales ($> 2°\times2°$ degrees spatial resolution), where strong windstress cools SST (Small et al. 2008). Our data sources have 1°×1° or better spatial resolution, so that they resolve the scales where mesoscale oceanic influence is likely to be present. In particular, the Bay of Bengal (Chen et al. 2012) and western Arabian Sea (Seo et al. 2008) have strong eddy activity that is likely to contribute to ocean control of the air-sea interaction regime. Ocean control arising from upper-ocean T/S structure and mixing is not limited to the mesoscales, and is instead expected at the much larger scales over which the fresh layer from monsoon runoff spreads.

b. Influence of Radiation

Typically, the FCL98 model is run with two forcing terms: atmospheric forcing, (represented by T_a) and oceanic forcing (represented by Q_o) with the atmospheric forcing appearing only in the turbulent heat flux (Equation 2). Radiative effects are represented by the linear relaxation of temperature anomalies. This representation is sufficient in extratropical applications of the model, where longwave cooling is expected to be the most important radiative effect in most instances. But in the tropics, other radiative transfers such as shortwave surface warming play a large role in the upper ocean heat budget and may need to be included in the underlying model. Radiative forcing anomalies other than longwave cooling would appear in Equation (2) as an extra stochastic term on the RHS. Thus, use of this method without such a term will see oceanic and radiative forcing as equivalent.

To assess the potential confounding effect due to radiative forcing in our regime calculations, we split the model stochastic flux forcing term as

$$Q = Q_o + Q_r \tag{9}$$

where Q_o is the intrinsic oceanic forcing of FCL98 and $Q_r = \omega_r r_r$ is an additional stochastic radiative term, with ω_r the strength of radiative forcing in W m^{-2} and r_r a Gaussian white noise process with mean 0 and standard deviation 1.

To separate the contribution of ocean and radiation to the SST tendency, we inspect the lagged correlation of SST and SST tendency anomalies with radiative heat flux anomalies in the model. The simultaneous correlation with SST tendency provides the necessary discrimination, giving the proportion of model stochastic forcing contributed by radiation rather than oceanic processes as:

$$C_{\mathrm{d}T_s/\mathrm{d}t,Q_{\mathrm{rad}}}(0) = \frac{\omega_r}{\sqrt{\omega_r^2+\omega_o^2}} \,. \tag{10}$$

Based on this reasoning from the model, we calculate this simultaneous correlation from observations, using the NASA CERES synoptic 1°×1° all-sky surface radiative fluxes (Rutan et al. 2015) together with the OISSTv1 SST used for the ASI regime calculations (Reynolds et al. 2007). The resulting correlation coefficients peak below 0.2 and drop off steeply above this value, showing that radiative forcing is not a strong contributor to the ASI regimes in our case. This justifies treating the radiative effect as a simple longwave cooling for qualitative seasonal analysis and leaving further improvement for future work.

An additional radiative influence on ocean control is the effect of penetrating shortwave radiation (Sengupta et al. 2002; Paulson and Simpson 1977). The mixed layer depth sets the portion of shortwave radiation absorbed in the mixed layer, which modifies the SST tendency so that two ocean columns can have differing SST tendencies with the same surface shortwave radiation. In this way, mixed layer depth is an additional contribution to ocean control of air-sea interaction.

c. ASI Regimes in Models

The ASI regime parameter P_o provides a diagnostic of air-sea interaction behavior that may be compared across models of varying complexity. In the simple model of FCL98, we may relate our ASI regimes to underlying physical drivers. To do so, we compare the calculated P_o to the squared ratio of stochastic forcing strengths $\omega_o^2/(\omega_o^2+\omega_a^2)$ used to drive the 1D model ((Fig. 7; see Equation 2). This ratio is one way that the underlying ocean and atmosphere drivers can be quantified, with a ratio near 0 indicating atmosphere control, while a ratio near 1 indicates ocean control. The parameter P_o contains all of the information of the forcing ratio: the two parameters have a monotonic relationship, allowing for retrieval of the forcing strength ratio from P_o through a lookup table. P_o better resolves the range of air-sea interaction regimes of interest, conveniently spreading its values over the range of conditions most frequently exhibited during the summer monsoon (Fig. 7, gray shading).

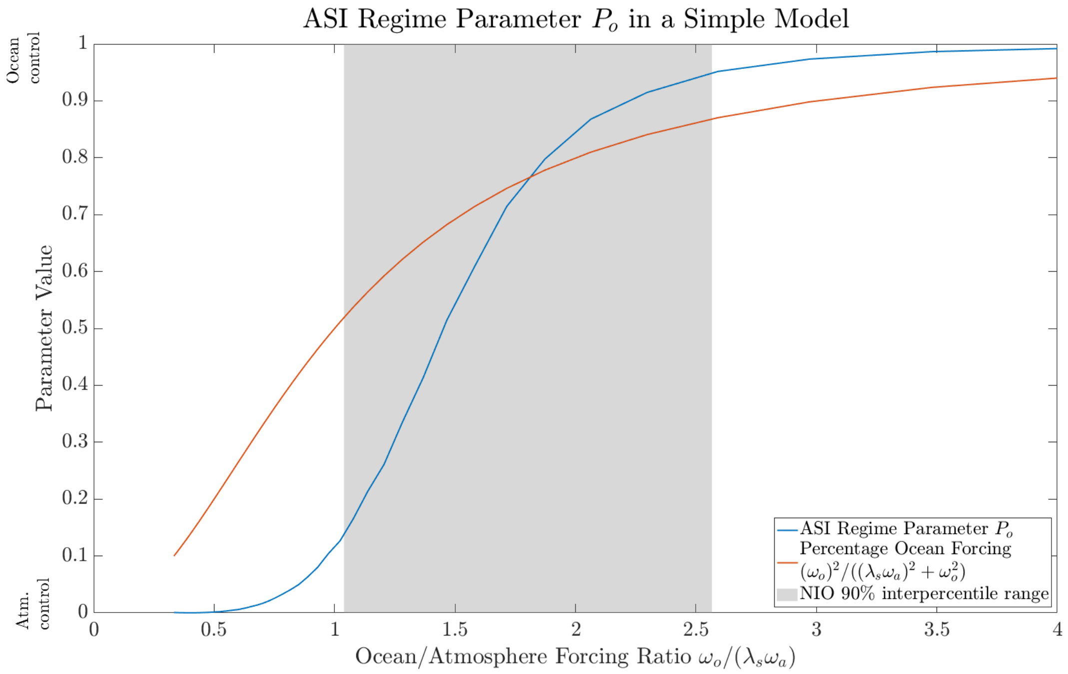

FIG. 7. Use of symmetry-derived ASI regime parameter P_o in a simple model. The parameter P_o is calculated in the FCL98 stochastic model (Equation 2) for a variety of ratios of oceanic forcing strengths (ω_o) to atmospheric forcing strengths ($\lambda_s\omega_a$). The squared proportion of oceanic forcing strength is plotted for comparison. Gray shading shows the 5th to 95th interpercentile range for the monthly climatological OAFlux ASI regimes in the NIO.

The forcing ratio $\omega_o/(\lambda_s\omega_a)$ is conveniently computed in simple models, but is ill-defined in fully coupled 3D models or in observations of the real earth system. The ASI regime parameter P_o, on the other hand, may be defined and measured for any coupled ocean-atmosphere system, modeled or observed. In this way, it provides a unified diagnostic to assess behavior across a range of scales and complexities. The values of P_o diagnosed from a coupled 3D model and compared to observations would provide a useful diagnostic for the model's representation of air-sea interaction drivers and couplings. For example, the seasonal histograms of Fig. 4 may be calculated from 3D model output in the same manner as from observations. If atmospheric control persists during the modeled summer monsoon season, this could suggest that ocean dynamics are being under-resolved in the model, such that the surface fluxes are over-controlled by surface air temperature or humidity. Such analyses may offer a fruitful diagnostic for model representations not just of the

South Asian summer monsoon, but also other coupled ocean and atmosphere phenomena across the globe.

5. Conclusion

In this work, we have introduced a new method to algorithmically determine the climatological daily air-sea interaction regime of a region, which separates the turbulent heat flux into an atmosphere-controlled and ocean-controlled contributions. We have applied this method to satellite and reanalysis-based datasets in the northern Indian Ocean and found that there is a pronounced shift in the air-sea interaction regime during the onset of the South Asian summer monsoon. The region's THF transitions from primarily atmosphere-controlled to ocean-controlled on a weekly timescale. This transition is partially due to the influence of increased wind stress which brings deep water to the surface through both mechanical mixing and buoyancy forcing. The Arabian Sea exhibits stronger and more rapid transitions of ASI regime than the Bay of Bengal because its upper-ocean thermodynamic structure is more conducive to changing SST in response to winds.

Our results highlight the importance of ocean temperature-salinity structure and mixing processes in the dynamics of the monsoon, with air-sea interaction at the interface controlled to a significant extent by the processes occurring in the ocean. In the realm of modeling the South Asian summer monsoon, our results emphasize the importance of improving ocean mixing schemes for development of monsoon forecasts, as the summer monsoon season is when ocean processes are most critical for the air-sea interaction of the region. The correlation between ASI regimes and windstress underscores the direct and indirect influence of winds on air-sea interaction, through controlling latent and sensible heat fluxes and also through enhancing ocean mixing and currents. More broadly, the ASI regime parameter framework offers a diagnostic to distill the dynamics of regions where the balance between ocean and atmosphere may fluctuate in space and time.

Acknowledgments. The authors are supported by the Office of Naval Research Arabian Sea Transition Layer (ASTraL) departmental research initiative under Grant N00014-23-1-2471. We also thank the Francis E. Fowler IV Center for Oceans and Climate at the Woods Hole Oceanographic Institution for a research award.

Data availability statement. OAFlux data is available from the Asia-Pacific Data-Research Center at`https://apdrc.soest.hawaii.edu/datadoc/whoi_oaflux.php`. ERA5 reanalysis is available from the Copernicus Data Store at `https://cds.climate.copernicus.eu/datasets/reanalysis-era5-complete`. Code for running the stochastic model, processing data, and generating figures is available on GitHub at `https://github.com/alexkinsella/asi_regimes`.

APPENDIX

Statistical Testing of Lagged Correlations

To ensure that our regime parameters remain physically relevant, we perform a series of statistical tests to de-emphasize insignificant correlations in our calculation while accounting for autocorrelation and multiple comparisons (Wilks 2011).

To test the daily lagged correlations for insignificant results, we resample the pool of T_s, $\mathrm{d}T_s/\mathrm{d}t$, and Q_{turb} observations to obtain 1000 synthetic time series. We calculate the lagged T_s-Q_{turb} and $\mathrm{d}T_s/\mathrm{d}t$-$Q_{\mathrm{turb}}$ correlations from these series and calculate the resulting PDF of the following sum of the largest correlations for each day and location:

$$\max_l \|C_{T_s,Q_{\mathrm{turb}}}(l)\| + \max_l \|C_{\mathrm{d}T_s/\mathrm{d}t,Q_{\mathrm{turb}}}(l)\| \,. \tag{A1}$$

We assume that when these maximum correlations are sufficiently small, the whole lagged correlation curve is the result of noise. For our resampled OAFlux dataset, this results in a threshold value of 0.194 for a 95% confidence interval. This flags only 0.23% of our observed lagged correlation curves as being due to noise. Because this proportion is so small, we leave all correlations unmasked without significantly affecting the results.

To introduce additional statistical testing, we calculate p-values for each lagged correlation to be used in the next step of the algorithm. To account for space-time autocorrelations in the measurements, we compute our p-values as follows. First, we compute naive p-values for each time series as if they were independent and identically distributed. These are then modified to *effective* p-values using the method of (Bretherton et al. 1999). This means that we calculate p-values using an effective number of degrees of freedom

$$N_{\text{eff}} = N \frac{1 - \rho_{T_s} \rho_{Q_{\text{turb}}}}{1 + \rho_{T_s} \rho_{Q_{\text{turb}}}}, \tag{A2}$$

where N is the number of observations in the correlation, ρ_{T_s} is the lag-1 autocorrelation of the SST anomaly time series and $\rho_{Q_{\text{turb}}}$ is the lag-1 autocorrelation of the turbulent heat flux anomaly time series.

After calculating the effective p-values for all times, grid points, and lags, we apply field significance testing to all of them together using the procedure of (Benjamini and Hochberg 1995). This corrects for the multiple comparisons problem by controlling the false discovery rate. The result is a set of q-values that represent the false discovery rate that would be required to reject the null hypothesis for each observation.

To de-emphasize low-confidence correlations in the least squares fit to determine the regime parameters in equation (8), we weight the least squares problem by a diagonal matrix W whose entries are weights

$$w(l) = 1 - \frac{1}{1 + \exp(-k(2q_{\text{eff}}(l) - 1))}, \tag{A3}$$

where $q_{\text{eff}}(l)$ are the q-values from the previous step and k is a steepness parameter that controls how sharply the weight drops off as q increases beyond 0.5. We choose $k = 5$; our results are not sensitive to the choice of k. The residual of the fit is always small, even for noise time series, so that a small residual on its own does not guarantee a physically meaningful decomposition.

References

Abbott, K., and A. Mahadevan, 2024: Why is the monsoon coastal upwelling signal subdued in the Bay of Bengal? *Journal of Geophysical Research: Oceans*, **129 (12)**, e2024JC022 023.

Barsugli, J. J., and D. S. Battisti, 1998: The basic effects of atmosphere–ocean thermal coupling on midlatitude variability. *Journal of the Atmospheric Sciences*, **55 (4)**, 477–493.

Benjamini, Y., and Y. Hochberg, 1995: Controlling the false discovery rate: a practical and powerful approach to multiple testing. *Journal of the Royal Statistical Society: Series B (Methodological)*, **57 (1)**, 289–300.

Bentamy, A., and Coauthors, 2017: Review and assessment of latent and sensible heat flux accuracy over the global oceans. *Remote Sensing of Environment*, **201**, 196–218.

Bishop, S. P., R. J. Small, F. O. Bryan, and R. A. Tomas, 2017: Scale dependence of midlatitude air–sea interaction. *Journal of Climate*, **30 (20)**, 8207–8221.

Bretherton, C. S., M. Widmann, V. P. Dymnikov, J. M. Wallace, and I. Bladé, 1999: The effective number of spatial degrees of freedom of a time-varying field. *Journal of Climate*, **12 (7)**, 1990–2009.

Chen, G., D. Wang, and Y. Hou, 2012: The features and interannual variability mechanism of mesoscale eddies in the Bay of Bengal. *Continental Shelf Research*, **47**, 178–185.

Edson, J. B., and Coauthors, 2013: On the exchange of momentum over the open ocean. *Journal of Physical Oceanography*, **43 (8)**, 1589–1610.

Frankignoul, C., 1985: Sea surface temperature anomalies, planetary waves, and air-sea feedback in the middle latitudes. *Reviews of Geophysics*, **23 (4)**, 357–390.

Frankignoul, C., A. Czaja, and B. L'Heveder, 1998: Air–sea feedback in the north atlantic and surface boundary conditions for ocean models. *Journal of Climate*, **11 (9)**, 2310–2324.

Frankignoul, C., and K. Hasselmann, 1977: Stochastic climate models, part II: Application to sea-surface temperature anomalies and thermocline variability. *Tellus*, **29 (4)**, 289–305.

Frankignoul, C., and E. Kestenare, 2002: The surface heat flux feedback, part I: Estimates from observations in the atlantic and the north pacific. *Climate Dynamics*, **19**, 633–647.

Frankignoul, C., E. Kestenare, M. Botzet, A. F. Carril, H. Drange, A. Pardaens, L. Terray, and R. Sutton, 2004: An intercomparison between the surface heat flux feedback in five coupled models, COADS and the NCEP reanalysis. *Climate Dynamics*, **22**, 373–388.

Gadgil, S., 2003: The Indian monsoon and its variability. *Annual Review of Earth and Planetary Sciences*, **31 (1)**, 429–467.

Goswami, B., S. A. Rao, D. Sengupta, and S. Chakravorty, 2016: Monsoons to mixing in the Bay of Bengal: Multiscale air-sea interactions and monsoon predictability. *Oceanography*, **29 (2)**, 18–27.

Hersbach, H., and Coauthors, 2020: The ERA5 global reanalysis. *Quarterly Journal of the Royal Meteorological Society*, **146 (730)**, 1999–2049.

Hobday, A. J., and Coauthors, 2016: A hierarchical approach to defining marine heatwaves. *Progress in Oceanography*, **141**, 227–238.

Jain, V., D. Shankar, P. Vinayachandran, A. Mukherjee, and P. Amol, 2021: Role of ocean dynamics in the evolution of mixed-layer temperature in the Bay of Bengal during the summer monsoon. *Ocean Modelling*, **168**, 101 895.

Laurindo, L. C., and Coauthors, 2022: Role of ocean and atmosphere variability in scale-dependent thermodynamic air-sea interactions. *Journal of Geophysical Research: Oceans*, **127 (7)**, e2021JC018 340.

Montégut, C. B., J. Vialard, S. S. Shenoi, D. Shankar, F. Durand, C. Ethé, and G. Madec, 2007: Simulated seasonal and interannual variability of the mixed layer heat budget in the northern Indian Ocean. *Journal of Climate*, **20 (13)**, 3249–3268.

Park, S., C. Deser, and M. A. Alexander, 2005: Estimation of the surface heat flux response to sea surface temperature anomalies over the global oceans. *Journal of Climate*, **18 (21)**, 4582–4599.

Paulson, C. A., and J. J. Simpson, 1977: Irradiance measurements in the upper ocean. *Journal of Physical Oceanography*, **7 (6)**, 952–956.

Prasad, T., 2004: A comparison of mixed-layer dynamics between the Arabian Sea and Bay of Bengal: One-dimensional model results. *Journal of Geophysical Research: Oceans*, **109 (C3)**.

Rao, R., M. G. Kumar, M. Ravichandran, A. Rao, V. Gopalakrishna, and P. Thadathil, 2010: Interannual variability of Kelvin wave propagation in the wave guides of the equatorial Indian ocean, the coastal Bay of Bengal and the southeastern Arabian Sea during 1993–2006. *Deep Sea Research Part I: Oceanographic Research Papers*, **57 (1)**, 1–13.

Rao, R., and R. Sivakumar, 2000: Seasonal variability of near-surface thermal structure and heat budget of the mixed layer of the tropical Indian Ocean from a new global ocean temperature climatology. *Journal of Geophysical Research: Oceans*, **105 (C1)**, 995–1015.

Reynolds, R. W., T. M. Smith, C. Liu, D. B. Chelton, K. S. Casey, and M. G. Schlax, 2007: Daily high-resolution-blended analyses for sea surface temperature. *Journal of Climate*, **20 (22)**, 5473–5496.

Rutan, D. A., S. Kato, D. R. Doelling, F. G. Rose, T. E. Caldwell, N. G. Loeb, and et al., 2015: CERES synoptic product: Methodology and validation of surface radiant flux. *Journal of Atmospheric and Oceanic Technology*, **32 (6)**, 1121–1143.

Schott, F. A., and J. P. McCreary Jr, 2001: The monsoon circulation of the Indian Ocean. *Progress in Oceanography*, **51 (1)**, 1–123.

Sengupta, D., P. K. Ray, and G. Bhat, 2002: Spring warming of the eastern Arabian Sea and Bay of Bengal from buoy data. *Geophysical Research Letters*, **29 (15)**, 24–1.

Seo, H., R. Murtugudde, M. Jochum, and A. J. Miller, 2008: Modeling of mesoscale coupled ocean–atmosphere interaction and its feedback to ocean in the western Arabian Sea. *Ocean Modelling*, **25 (3-4)**, 120–131.

Shenoi, S., D. Shankar, and S. Shetye, 2002: Differences in heat budgets of the near-surface Arabian Sea and Bay of Bengal: Implications for the summer monsoon. *Journal of Geophysical Research: Oceans*, **107 (C6)**, 5–1.

Small, R. d., and Coauthors, 2008: Air–sea interaction over ocean fronts and eddies. *Dynamics of Atmospheres and Oceans*, **45 (3-4)**, 274–319.

Thakur, R., E. L. Shroyer, R. Govindarajan, J. T. Farrar, R. A. Weller, and J. N. Moum, 2019: Seasonality and buoyancy suppression of turbulence in the Bay of Bengal. *Geophysical Research Letters*, **46 (8)**, 4346–4355.

Thangaprakash, V., and Coauthors, 2016: What controls seasonal evolution of sea surface temperature in the Bay of Bengal? mixed layer heat budget analysis using moored buoy observations along 90 E. *Oceanography*, **29 (2)**, 202–213.

Vecchi, G. A., and D. Harrison, 2002: Monsoon breaks and subseasonal sea surface temperature variability in the Bay of Bengal. *Journal of Climate*, **15 (12)**, 1485–1493.

von Storch, J.-S., 2000: Signatures of air–sea interactions in a coupled atmosphere–ocean GCM. *Journal of Climate*, **13 (19)**, 3361–3379.

Warner, S. J., J. Becherer, K. Pujiana, E. L. Shroyer, M. Ravichandran, V. Thangaprakash, and J. N. Moum, 2016: Monsoon mixing cycles in the Bay of Bengal: A year-long subsurface mixing record. *Oceanography*, **29 (2)**, 158–169.

Weller, R. A., and Coauthors, 2016: Air-sea interaction in the Bay of Bengal. *Oceanography*, **29 (2)**, 28–37.

Wilks, D. S., 2011: *Statistical methods in the atmospheric sciences*, Vol. 100. Academic press.

Wu, R., B. P. Kirtman, and K. Pegion, 2006: Local air–sea relationship in observations and model simulations. *Journal of Climate*, **19 (19)**, 4914–4932.

Yu, L., and R. A. Weller, 2007: Objectively analyzed air–sea heat fluxes for the global ice-free oceans (1981–2005). *Bulletin of the American Meteorological Society*, **88 (4)**, 527–540.